STRUCTURE AND DEFORMATION OF GRADIENT METAL FOAMS PRODUCED BY

**MACHINING** 

Haipeng Qiao<sup>1</sup>, Tejas G. Murthy<sup>2</sup>, Christopher Saldana<sup>1,\*</sup>

<sup>1</sup>George W. Woodruff School of Mechanical Engineering, Georgia Institute of Technology

Atlanta, GA

<sup>2</sup>Department of Civil Engineering, Indian Institute of Science, Bangalore, India

\*Corresponding Author: christopher.saldana@me.gatech.edu, +1.404.385.3735

**ABSTRACT** 

The effects of surface structure on mechanical performance for open-cell aluminum foam

specimens was investigated in the present study. A surface gradient for pore structure and diameter

was introduced into open cell aluminum foams by machining-based processing. The structure

changes in the strut and pore network were evaluated by computed tomography characterization.

The role of structure gradients in affecting mechanical performance was determined using digital

volume correlation and in situ compression within the computed tomographic scanner. These

preliminary results show that the strength of these materials may be enhanced through surface

structural gradients.

**Keywords**: Foams, Machining, Tomography

MANU-19-1273 Saldana 1

#### INTRODUCTION

Metallic open cell foams are an important class of solids used across a range of applications including lightweighting, energy absorption and high temperature filtration applications. Low density cellular metals can extend the design space and provide for enhanced product performance by system lightweighting, enhanced impact absorption and high temperature media filtration. For biomedical implants, low density cellular metals are important materials for next generation fixation implants as they dramatically improve the quality of trauma fixation, as well as resulting quality-of-life, relative to conventional fully-dense bulk metallic implants.

Material response in manufacturing processes used to bring cellular metals to final form has primarily been empirical in nature [1-9]. Deformation occurring in surface generation by machining of these materials differs substantially than in simple compression due to the heterogeneous nature of the deformation present during surficial deformation. This heterogeneity is known to cause spatially-dependent damage in the immediate surface as well as a range of diffuse and localized structure damage throughout the subsurface (e.g., banding, cell damage, dilation) [9-13]. More recently, studies have provided more comprehensive characterization of machining-induced effects on damage/change to foam structure [14, 15], however the effects of these structure changes are not yet elucidated in terms of material performance.

The goal of the present study is to establish an understanding of the role of machining parameters in determining the final structure of machined foam surfaces. Further, compression tests were conducted to determine how these structure changes affect mechanical performance. A series of

in situ compression tests were carried out within a tomographic scanning environment to enable full 3-D characterization of the deformation field using digital volume correlation (DVC).

### **EXPERIMENTAL**

Milling open-cell aluminum foams (Duocel 6101-T6) was done using a face milling tool (50 mm diameter) with uncoated carbide inserts. Machined samples were produced under various conditions for cutting speeds, feed rates, and axial depths of cut; these conditions are shown in Table 1. To characterize structure, a micro-computed tomography platform (Zeiss Metrotom) was utilized for full-volume structural characterization at 50.94 um/voxel. During the tomographic scans, the workpiece was rotated incrementally over a total angular range as image projections were acquired. The X-ray tube was used under controllable power settings and the X-ray beam directed through the sample and onto a planar detector. By collecting a large number of projections from different orientations of the sample in front of the detector, the Feldkamp-type cone-beam filtered back projection reconstruction provided 3D map of the effective attenuation coefficients within the sample, in terms of gray levels corresponding to the average density inside each voxel. This map formed the 3D image and individual 2D image slices of the solid corresponding to unit voxel thickness. An ISO50 threshold was used for this purpose, this threshold is defined by the average values for each of the air and solid phases and subsequent binarization facilitated distinction between the aluminum and pore space to create 3D volumetric renderings, pore detection using watershed segmentation and skeletonization of the network by median extraction.

A MATLAB-based 3D watershed algorithm was used to isolate and quantitatively characterize pore morphology. The analysis code assigns labels to pores using a volumetric distance map wherein each voxel's distance to the closest solid-phase voxel is determined and the pore centroid is found at a local peak. DVC was used to quantitatively measure the deformation field. This image correlation technique allows for full 3D strain measurement of a deforming solid. In order to characterize the cell and strut morphology, and subsequently observe the in situ internal microstructure evolution after each compressive step, the loading stage was mounted on the rotational stage between the X-ray source and the detector in the micro-computed tomography platform. This facilitated in situ scanning of the foam during loading.

## **DVC MEASUREMENT VALIDATION**

In this study, simulated translation and uniform compression displacement fields were evaluated with various grid sizes  $GS = \{13, 19, 25\}$  voxels and sub-volume sizes  $SS = \{51, 75, 99\}$  voxels. A test volume filled with spherical particles was utilized to determine the accuracy of the DVC code implementation. The predefined displacement values were  $\{0, 0.4, 0.8, 1.6, 3.2, 4, 8, 12, 16, 20, 24\}$  voxels and strain values were  $\{2\%, 4\%, 6\%\}$ . The test results are plotted in Figure 1. The mean bias (error) of integer voxel displacement is in the order of  $1.0 \times 10$ -6 voxels, and insensitive to the different grid and sub-volume sizes. In contrast, the bias from sub-voxel displacement can reach up to  $1.0 \times 10$ -5 voxels, ten times greater than in the integer displacement cases. Basically, small deformation and large sub-volume size gave rise to high accuracy and precision, which are insensitive to the grid spacing. In addition, the standard deviation changed linearly with the input strain, and a large sub-volume yielded a low slope, this indicating that the precision was relatively stable to parameters.

The artificial deformation tests on ideal 3D images help to quantify the uncertainties from DVC itself. However, in experiment, images are collected from real CT machines and this may provide an additional source of uncertainty. Thus, it was necessary to evaluate the uncertainty by applying the artificial deformation to the real reconstructed images with a known solution as in Fig. 2. Two consecutive scans on a foam sample were conducted under the same settings as in the experiment discussed in the ensuing, and the artificial deformation was applied to one of the two baseline images by calculating the analytical displacement field at each voxel and evaluating it based on spline interpolation in MATLAB.

The DVC was performed on the image pair to generate quantitative results. The representative image pairs for artificial translation and compression were rendered and inset in Fig. 2. The test results are also shown in Fig. 2. From the figure, the mean bias of displacement was relative constant in the order of 3.3 x 10-2 voxels. The mean bias was higher than in the case of the spheres in Fig. 1, presumably due to the marker field characteristics. Figure 2 also indicates that the mean bias was relatively constant for different input nominal compressive strain. As expected, a larger sub-volume yielded high accuracy and precision.

### RESULTS AND DISCUSSION

The effect of the machining process on subsurface structure is shown in Fig. 3, which details the evolution of the pore size versus the subsurface machined depth for different experimental conditions summarized in Table 1. Each pore was characterized by its centroid, which was located by the watershed segmentation algorithm. The pore diameter was evaluated by approximating the pore as a sphere, where volume is given by sum of the number of pore voxels based on the unique

labels resultant from watershed segmentation and multiplying by the volume of one voxel. Similarly, pore surface area was calculated by summing the boundary voxels for each marked region.

The extent of the machining-affected layer was evaluated based on the pore diameter of the bulk (undeformed) and machined (deformed) foam samples. For example, in Figure 3, the pores for an initial aluminum foam had a 2.2 mm diameter. The foam structure up to a subsurface depth of 2.8672 mm was modified by the surface generation process while material further away from the surface of the work material remained unaffected by deformation. In the proximity of the machined surface, the equivalent pore diameter decreased to approximately 0.5 mm because of deformations (e.g., fracture and bending). These effects were evident in the morphological evolution of the sets of pores identified in Fig. 3 as pairs A-A' and B-B'. In the deformation zone, pore A deformed substantially and decreased in size to A'. In contrast, pair B and B' in the far field exhibited no evidence of deformation or size changes. For test condition 2, the initial foam again had an effective pore size of 2 mm, and this pore size was 0.5 mm near the surface. Compared to the size of the deformation zone under test condition 1, the size of this zone under test condition 2 increased to roughly 3.6123 mm. Finally, for test condition 3, the machining affected layer increased to 4.0172 mm with a steady-state pore size of 0.5 mm.

Figure 3 demonstrates that the deformation zone increased as the depth of cut increased. Similarly, deformation zone extent increased together with higher feed and decreasing cutting speed, as shown in Fig. 4 and 5, respectively. For all conditions, as the distance into the bulk of the sample increased, the effective pore diameters of the machined samples approached those of the initial

bulk samples and pore surface area showed consistent pattern, this implying that the deformation could be characterized by either measurement. From this data, it is clear that the lowest cutting speed caused up to four layers of structural cell units of the foam to be affected by surface milling wherein the machined sample thickness contained a total of five layers. In contrast, the lowest feed restricted the deformation zone extent to one layer, regardless of the cutting speed used.

Figure 6 and Fig. 7 summarize two measurements of the strut deformation for a select number of experimental conditions. In the first row of each figure, the specific surface area of the foam was determined. This quantity is generally utilized to characterize permeability of cellular materials and is defined as external strut surface area per unit bulk volume. It can be expected that strut fracture yields new surface formation and an increase of this specific surface area. Under all test conditions, the specific surface area increases in a zone approximately a single unit cell level in extent, this indicating that only one layer of the foam opens to fracture after the face-milling process. In the second row of Fig. 6 and Fig. 7, stereographic projections are provided to summarize the final strut orientation distributions. These pole figures were calculated using the fixed node and midpoint in each strut segment. From the figures, the strut orientations in the original samples had no preferred orientations (e.g., random). In comparison, the machined surface struts were found to be highly concentrated in the sample normal direction (ND).

The mechanical performance of the aluminum foam specimens was investigated using compression tests on samples 10 mm x 10 mm x 16 mm. The nominal stress-strain curves were obtained from recorded load and displacement values from the compression test and are provided in Fig. 8. In the figure, the points I-IV and I'-IV' correspond to the points in (a)-(d) and (e)-(h),

respectively. In the case of the bulk foam specimen, the stress – strain relation is shown using the blue curve. This response exhibited an initial linear elastic regime with constant modulus of 29.27 MPa, a plateau up to 30% strain where most of the cells were deformed, and a densification where sustained deformation resulted in a rapid increase in stress due to compaction of the densified microstructure. The measured stress – strain curve for the machined specimen with a structure gradient, corresponding to Condition 5 in Table 1, exhibited the same general behavior, however with a linear elastic region with a higher constant modulus of 40.65 MPa and a peak yield stress of 1.01 MPa, a plateau with higher stresses than the bulk foam specimen, and a hardening regime wherein the mechanical response was found to coincide well with that of the bulk foam specimen. Figure 8 summarizes tomographic scans obtained to map the deformation evolution of bulk and machined foam specimens as compression progressed. To quantitatively determine the motion of struts in the bulk aluminum foam sample between successive imaging frames, the inter-frame xdirection, y-direction, z-direction and resultant displacement fields were computed by DVC. From the displacement fields, inter-frame strain fields were evaluated and are provided in Fig. 9 for both the bulk foam and machined foam samples. At the initial stages of the deformation, the maximum incremental strain was minimal. As deformation continued, deformation localized near initiation site of the first deformation band. At later stages of deformation, high values of incremental strain up to 10% were observed. The primary differences between the two foam samples was observed to be a slightly different plastic accommodation within the deformation band in Fig. 9(b) and Fig. 9(f). In the case of the latter, the deformation band is inclined at an angle of 20° from horizontal orientation. These differences in the incremental strain field are indicative of differences in the measured stress-strain response for both samples. Ongoing efforts are being made to further elucidate the role of local plastic accommodation differences in the pore and strut network to

macroscopic differences in apparent load response for the gradient and bulk foams. These efforts will be described in follow on investigations on plastic response of the foam samples.

## **CONCLUSIONS**

In the present study, surface structure deviations were introduced on foam samples by machining-based processing. The role of these structure changes on mechanical performance were evaluated. Tomographic investigation of structure was used to quantify these structure gradients as well as the evolution of the plastic field during compression of the foam samples. Digital volume correlation identified differences in the plastic field for these samples and load measurements showed that the gradient foams had a higher failure stress compared to the bulk foam samples. These results are potentially important for being able to design lightweight materials with enhanced mechanical performance through the use of structural gradation.

### **ACKNOWLEDGEMENTS**

Partial support of this work was from CMMI 1825640 and CMMI 1254818 (NSF). TM acknowledges the Fulbright-Nehru fellowship for funding.

### REFERENCES

 O. R. Tutunea-Fatan, M. A. Fakhri, and E. V. Bordatchev, "Porosity and cutting forces: from macroscale to microscale machining correlations," Proceedings of the Institution of Mechanical Engineers Part B-Journal of Engineering Manufacture, vol. 225, pp. 619-630, May 2011.

- J. Schoop, I. S. Jawahir, T. J. Balk, D. Busbaher, "High Performance Infiltrant-free Cryogenic Machining of 82% Density Porous Tungsten under Computer Numerical Control," in 15th IEEE International Vacuum Electronics Conference, Monterey, CA, 2014, pp. 167-168.
- 3. F. Pusavec, "Porous tungsten machining under cryogenic conditions," International Journal of Refractory Metals & Hard Materials, vol. 35, pp. 84-89, Nov 2012.
- 4. M. A. Fakhri, E. V. Bordatchev, and O. R. Tutunea-Fatan, "Framework for evaluation of the relative contribution of the process on porosity-cutting force dependence in micromilling of titanium foams," Proceedings of the Institution of Mechanical Engineers Part B-Journal of Engineering Manufacture, vol. 227, pp. 1635-1650, Nov 2013.
- M. A. Fakhri, E. V. Bordatchev, and O. R. Tutunea-Fatan, "An image-based methodology to establish correlations between porosity and cutting force in micromilling of porous titanium foams," International Journal of Advanced Manufacturing Technology, vol. 60, pp. 841-851, Jun 2012.
- M. Deglurkar, D. T. Davy, M. Stewart, V. M. Goldberg, and J. F. Welter, "Evaluation of machining methods for Trabecular Metal implants in a rabbit intramedullary osseointegration model," Journal of Biomedical Materials Research Part B-Applied Biomaterials, vol. 80B, pp. 528-540, Feb 2007.
- 7. S. Chen, D. Head, M. Effgen, and I. S. Jawahir, "An investigation of sustained machining performance for controlled surface quality requirements in porous tungsten," IEEE Transactions on Electron Devices, vol. 52, pp. 903-908, May 2005.
- 8. M. Bram, C. Kempmann, A. Laptev, D. Stover, and K. Weinert, "Investigations on the machining of sintered titanium foams utilizing face milling and peripheral grinding," Advanced Engineering Materials, vol. 5, pp. 441-447, Jun 2003.

- 9. R. G. Silva, U. Teicher, A. Nestler, and A. Brosius, "Finite element modeling of chip separation in machining cellular metals," Advanced Manufacturing, February 2015.
- 10. J. Schoop, M. Effgen, T. J. Balk, and I. S. Jawahir, "The effects of depth of cut and pre-cooling on surface porosity in cryogenic machining of porous tungsten," Procedia CIRP, vol. 8, pp. 357-362, 2013.
- 11. J. Schoop, M. Effgen, T. J. Balk, and I. S. Jawahir, "Improved product quality and resource efficiency in porous tungsten machining for dispenser cathode application by elimination of the infiltration process," in Re-engineering Manufacturing for Sustainability, pp. 241-244, 2013.
- 12. U. Teicher, and A. Nestler, "A method to simulate structural properties of cellular materials for machining processes," Proceedia CIRP, vol. 8, pp. 100–104, 2013.
- 13. P. S. Nebosky, S. R. Schmid and M. A. Sellés, "The springback characteristics of a porous tantalum sheet-metal," Journal of Manufacturing Science and Engineering, vol. 133.6, pp. 061022, 2011.
- 14. H. Qiao, S. Basu, S. Kumara, C. Saldana, "Subsurface damage in milling of lightweight open-cell aluminum foams," CIRP Annals, 2017, Vol. 66, pp. 125-128.
- 15. H. Qiao, S. Basu, C. Saldana, "Surface and subsurface microstructural damage in machining of porous metallic foams," Procedia CIRP, 45, pp. 335-338, 2016.

## **TABLE CAPTIONS**

Table 1. Experimental machining conditions where vc indicates cutting speed, vf is the table feed speed and ap is the depth of cut.

### FIGURE CAPTIONS

Figure 1. Simulated displacement/compression of test spheres: (a) mean bias of various displacements, (b) mean bias of strain levels under different grid and sub-volume settings on artificial 3D images.

Figure 2. Simulated displacement/compression of a metal foam: (a) mean bias of various displacements, (b) mean bias of strain levels under different grid and sub-volume settings on artificial 3D images.

Figure 3. Pore diameter and surface area vs subsurface machined depth for (a) Test 1, (b) Test 2, (c) Test 3.

Figure 4. Pore diameter and surface area vs subsurface machined depth for (a) Test 2, (b) Test 4, (c) Test 5.

Figure 5. Pore diameter and surface area vs subsurface machined depth for (a) Test 2, (b) Test 6, (c) Test 7.

Figure 6. Specific strut surface area vs subsurface machined depth for (a) Test 1 (b) Test 2, (c) Test 3 with corresponding strut branch orientation density variations in original samples (upper) and machined samples (lower).

Figure 7. Specific strut surface area vs subsurface machined depth for (a) Test 2, (b) Test 4, (c) Test 5 with corresponding strut branch orientation density variations in original samples (upper) and machined samples (lower).

Figure 8. Stress-strain curves in compressions of tests. CT scans from compression on (a)-(d) bulk and (e)-(h) machined foam samples. Sample width was 10 mm and images shown is taken at the midplane.

Figure 9. Incremental strain fields from in situ compression tests on (a)-(d) bulk foam and (e)-(h) machined foam samples. Sample width was 10 mm.

# **TABLES**

Table 1

Test	Vc	Vf	$a_p$
	(m/s)	(mm/min)	(mm)
1	2.6	0.051	1.0
2	2.6	0.051	1.5
3	2.6	0.051	2.0
4	2.6	0.102	1.5
5	2.6	0.204	1.5
6	3.7	0.051	1.5
7	5.2	0.051	1.5

# **FIGURES**

Figure 1

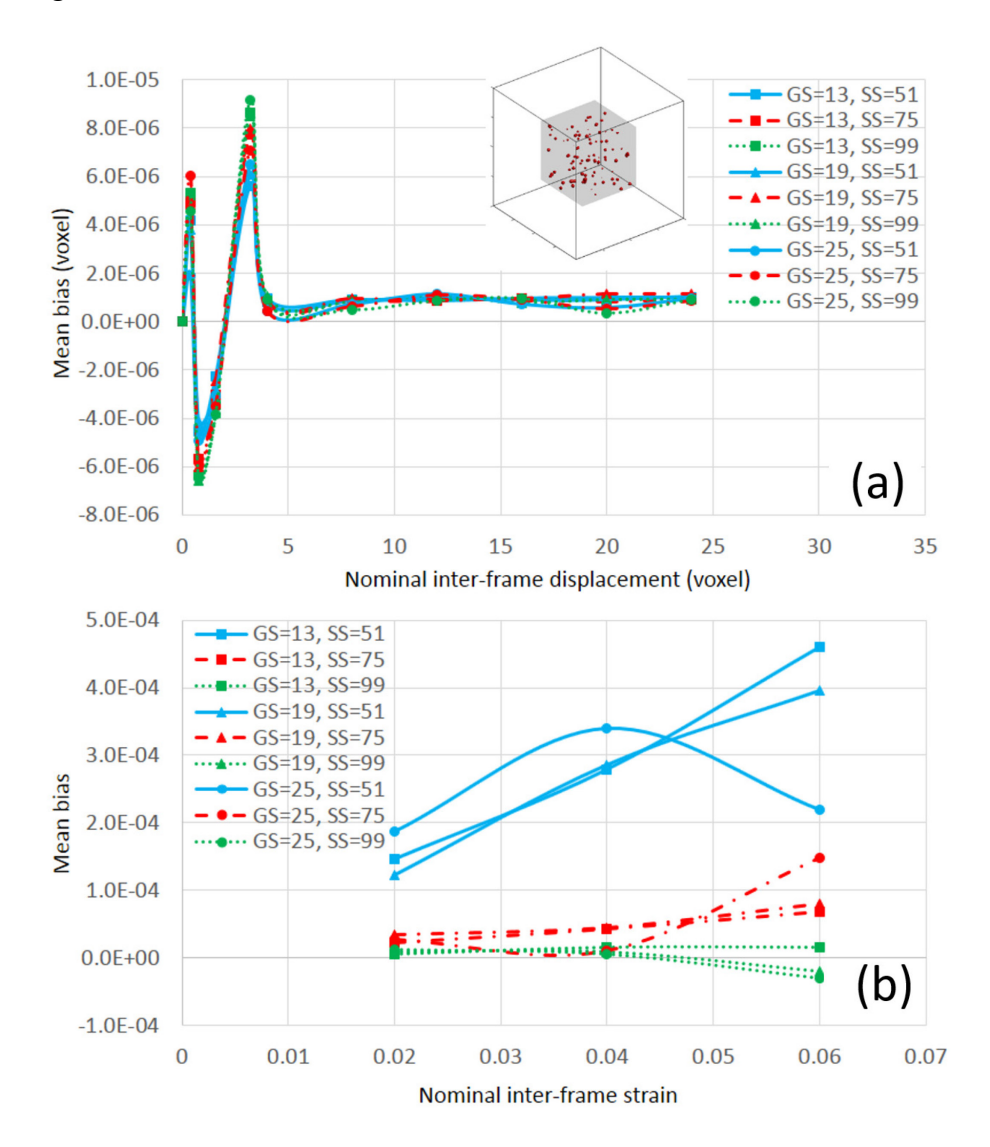


Figure 2

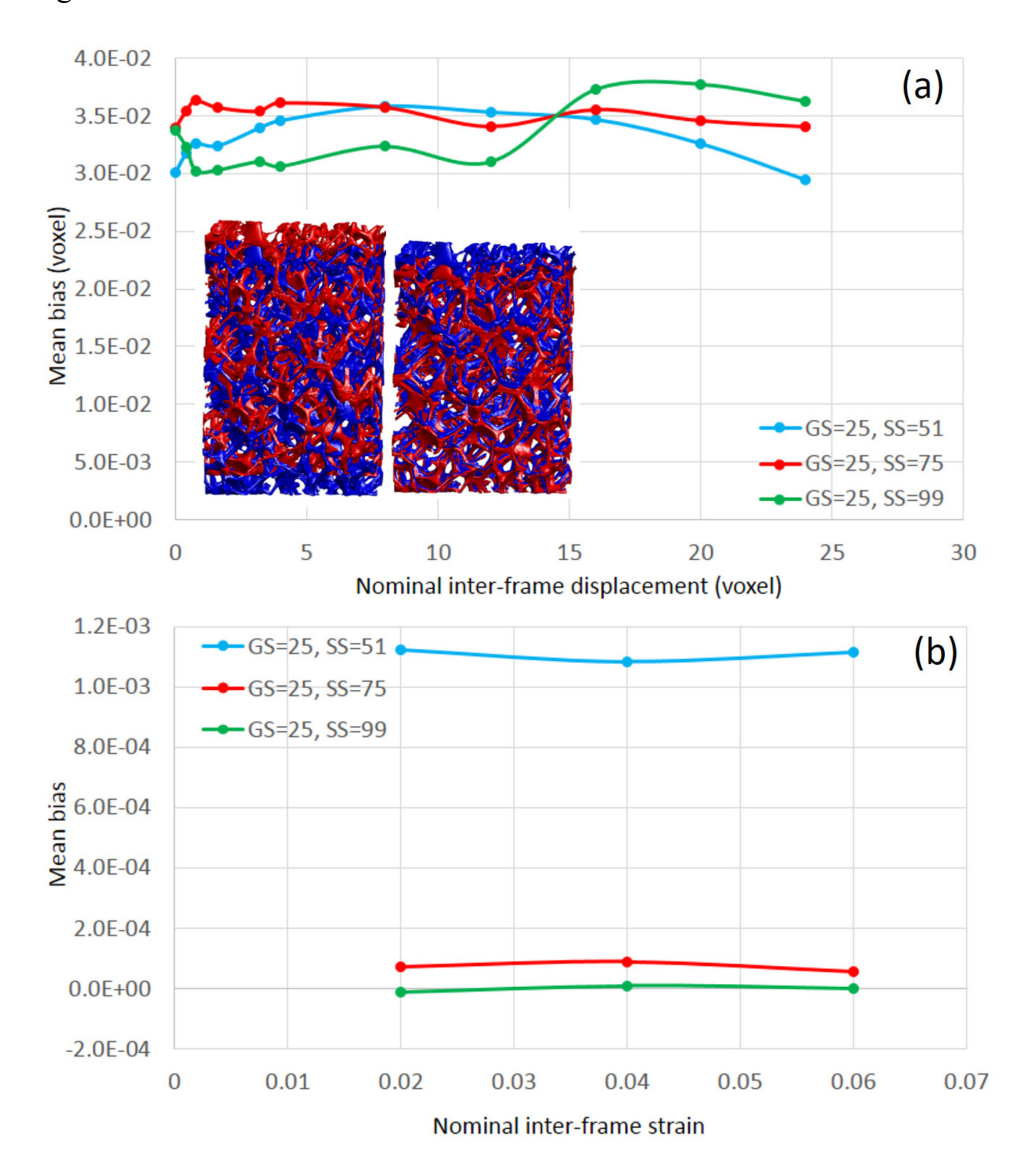


Figure 3

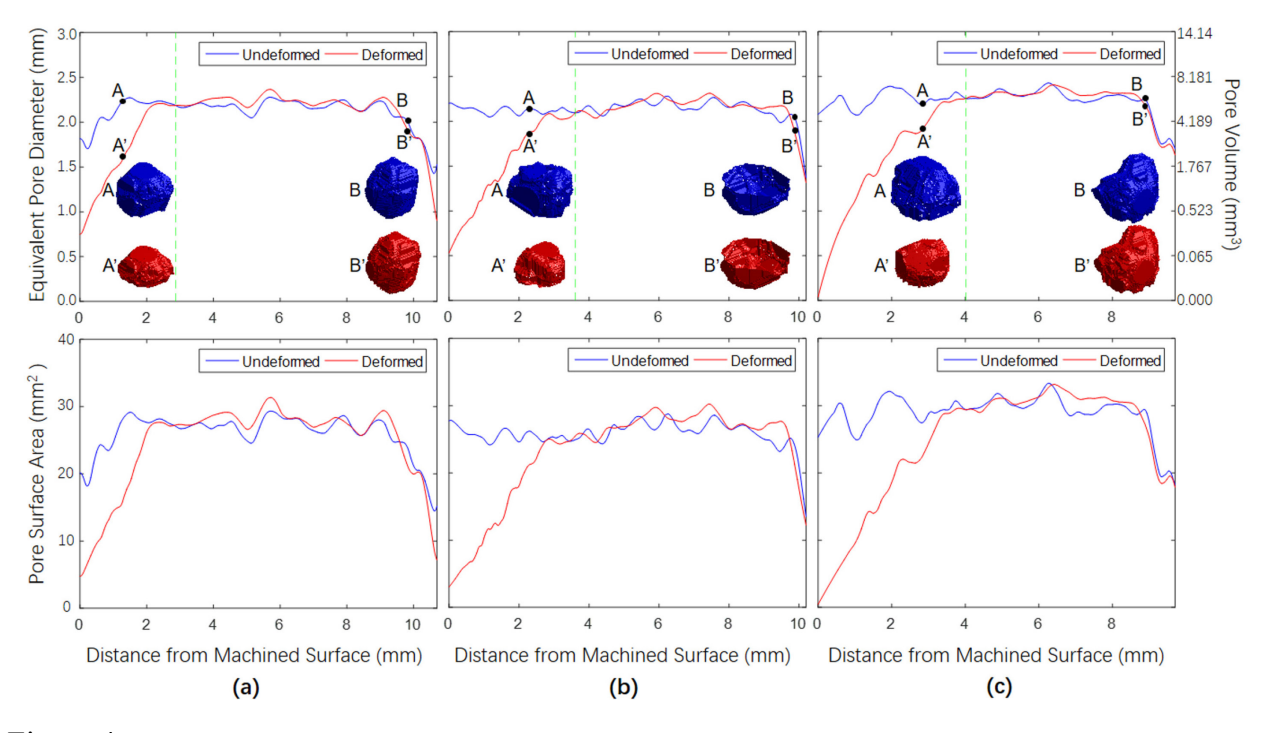


Figure 4

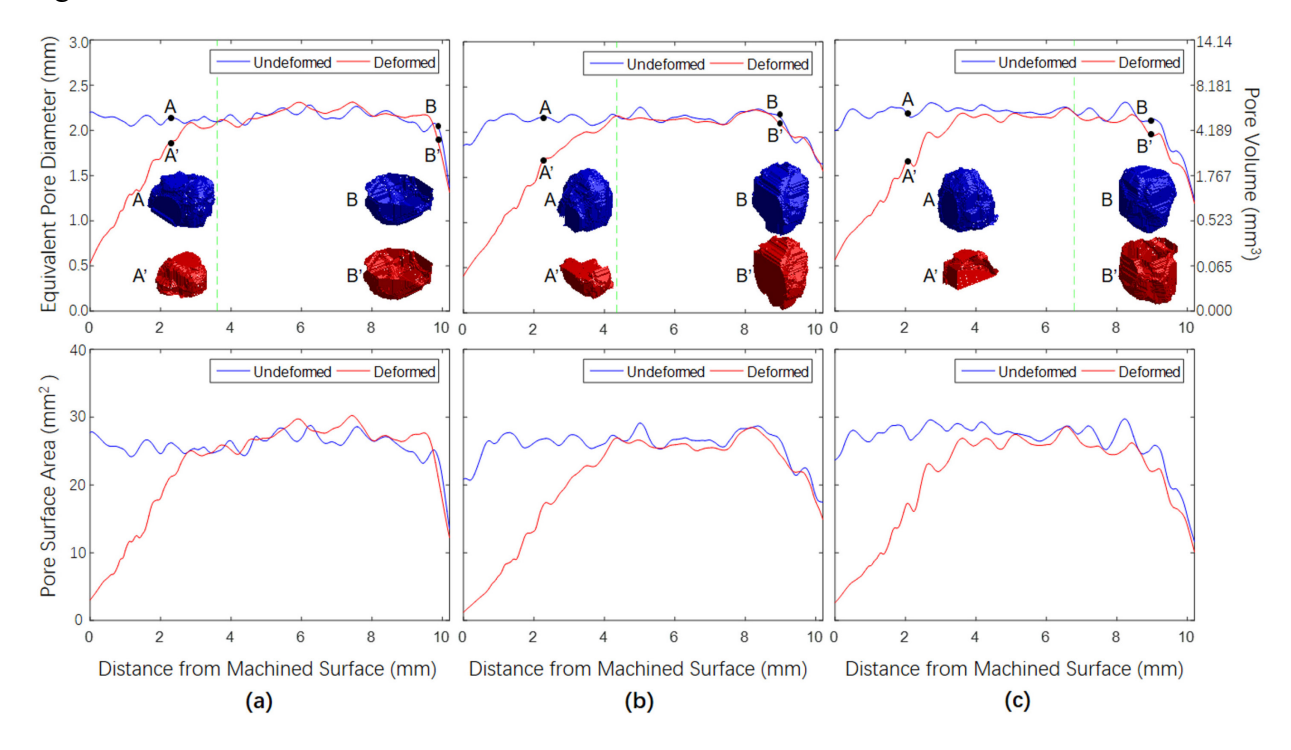


Figure 5

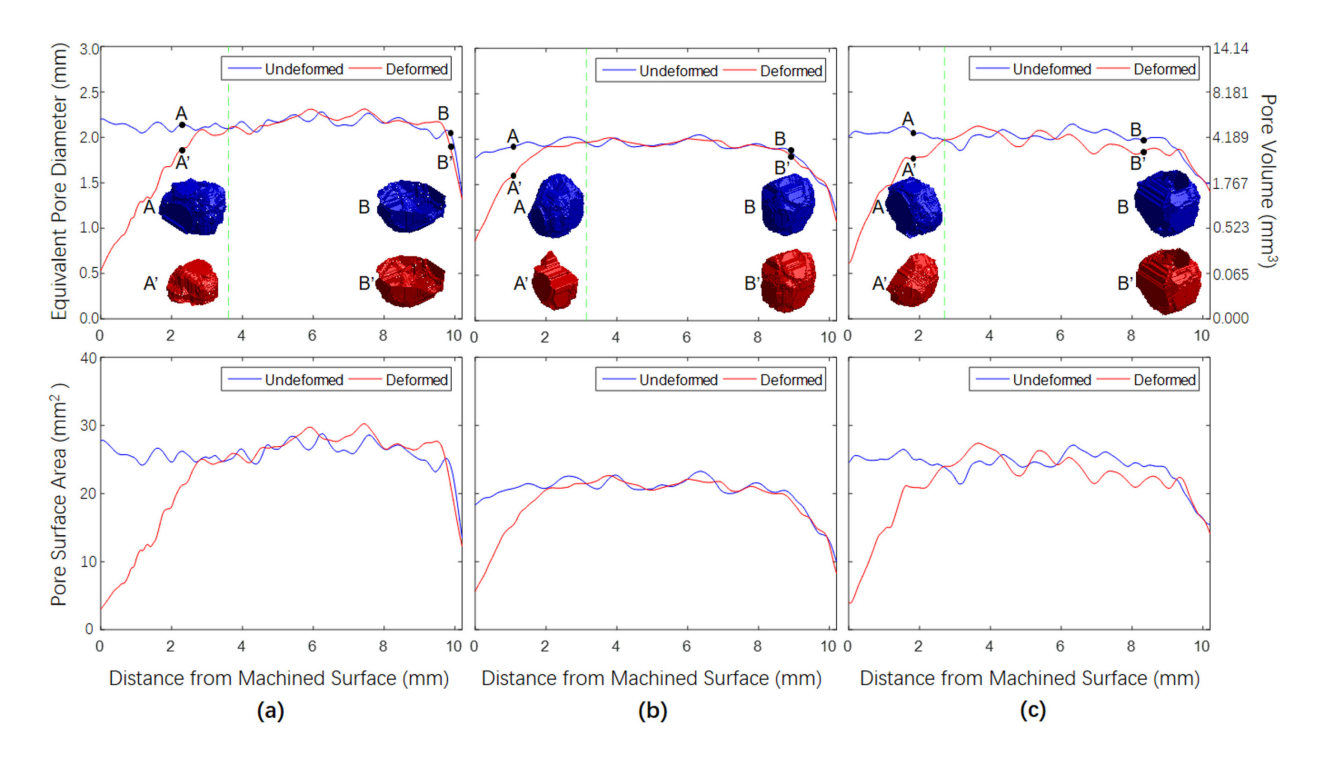


Figure 6

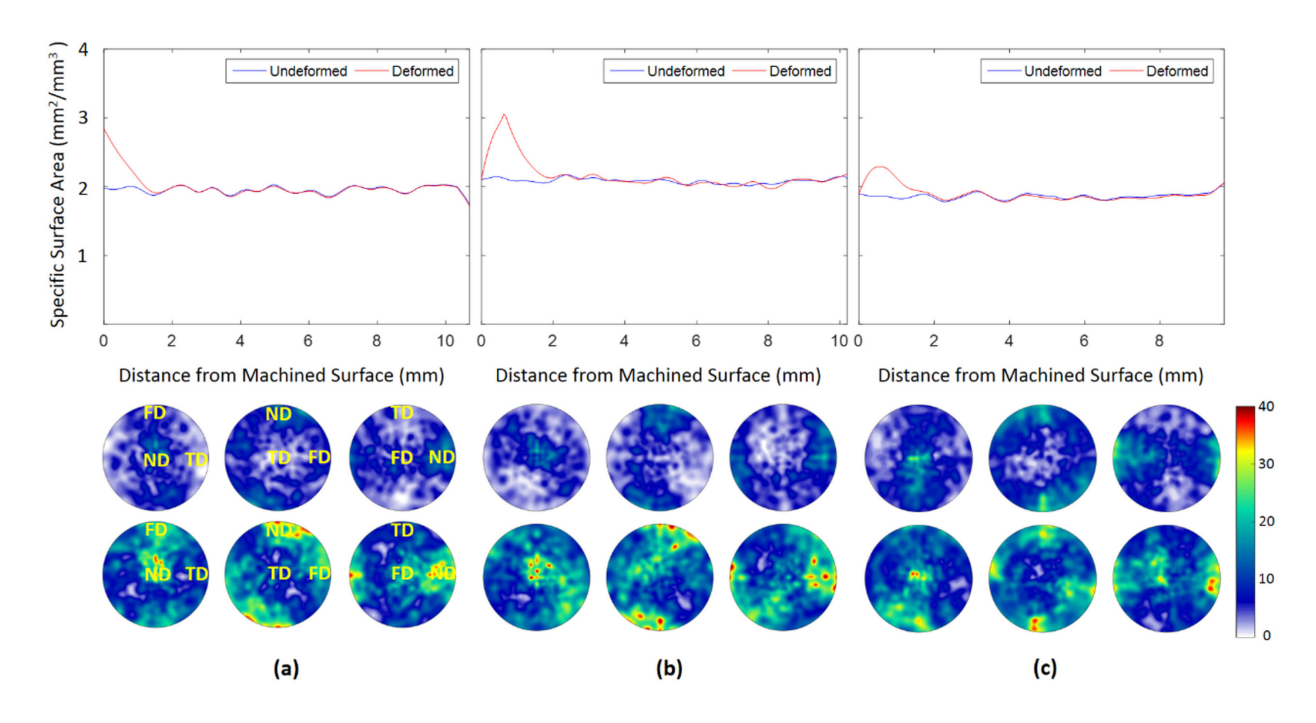


Figure 7

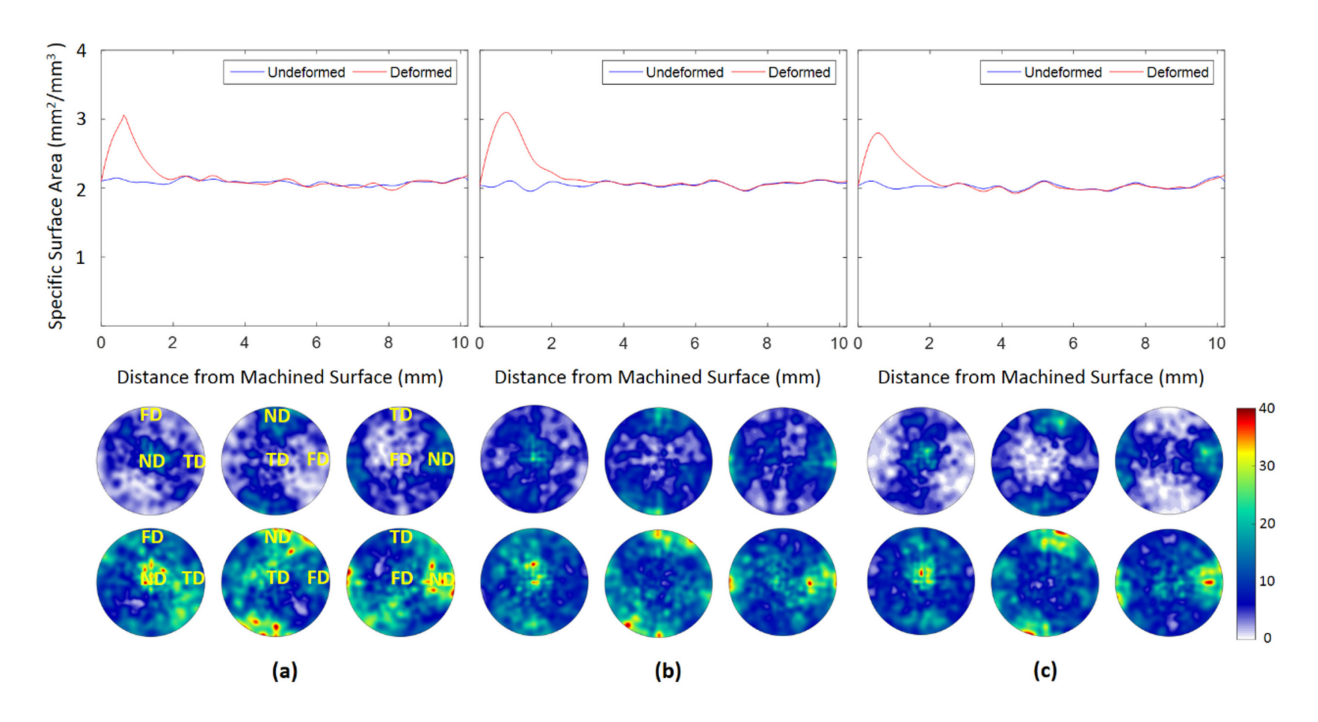


Figure 8

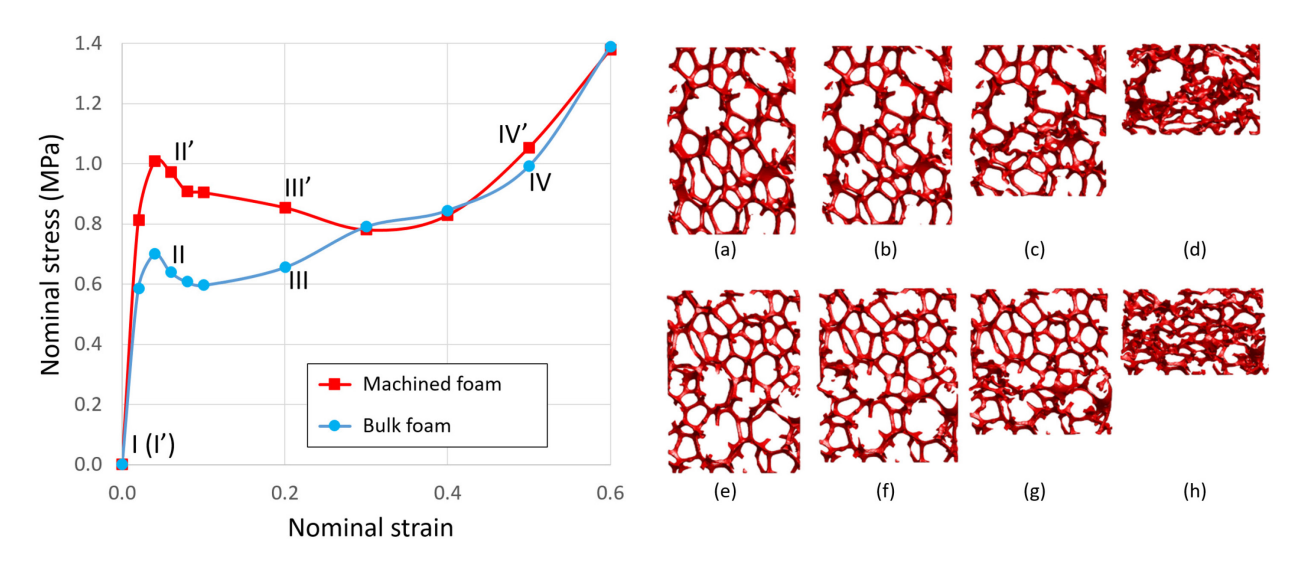


Figure 9

